Supplementary Information for: Tip-induced and electrical control of the photoluminescence yield of monolayer WS_2

Ricardo Javier Peña Román,[†,‖] Rémi Bretel,[‡,‖] Delphine Pommier,[‡,‖] Luis Enrique Parra López,[¶] Etienne Lorchat,[§] Elizabeth Boer-Duchemin,[‡] Gérald Dujardin,[‡] Andrei G. Borisov,[‡] Luiz Fernando Zagonel,[†] Guillaume Schull,[¶] Stéphane Berciaud,[¶] and Eric Le Moal[*,‡]

†*Institute of Physics "Gleb Wataghin", Department of Applied Physics, State University of Campinas-UNICAMP, 13083-859, Campinas, Brazil*

‡*Université Paris-Saclay, CNRS, Institut des Sciences Moléculaires d'Orsay, 91405, Orsay, France*

¶*Institut de Physique et de Chimie des Matériaux de Strasbourg, Université de Strasbourg, CNRS, IPCMS, UMR 7504, F-67000 Strasbourg, France*

§*NTT Research, Inc., Physics & Informatics (PHI) Laboratories, Sunnyvale, CA 94085, USA*

‖*These authors contributed equally to this work.*

E-mail: eric.le-moal@universite-paris-saclay.fr

Phone: +33 (0)1 69 15 66 97. Fax: +33 (0)1 69 15 67 77

S1 Extended data set used for Figure 1

Figures S1 and S2 show the extended data set from which the optical microscopy images shown in Figure 1 of the paper are taken. In both Figs. S1 and S2, white-light transmission microscopy images and wide-field laser-induced PL microscopy images of the same area of the sample are shown in panels (a) to (f) and panels (g) to (l), respectively. The STM tip is vertically withdrawn (several micrometers away from the surface) in the images of panels (a) and (g) and is engaged (i.e., in tunnel regime with closed feedback loop) in the images of the other panels. The shadow of the STM tip in the white-light transmission microscopy images shown in panels (b) to (f) reveals the lateral position of the tip apex on the sample (see the dark spot). Dotted lines (in red) delineate the flake domain above which the tip is placed. An arrow (in red) is added to guide the eye to the flake domain and the tip position. Sample bias is 1.5 V and setpoint current is 1 nA, except otherwise specified.

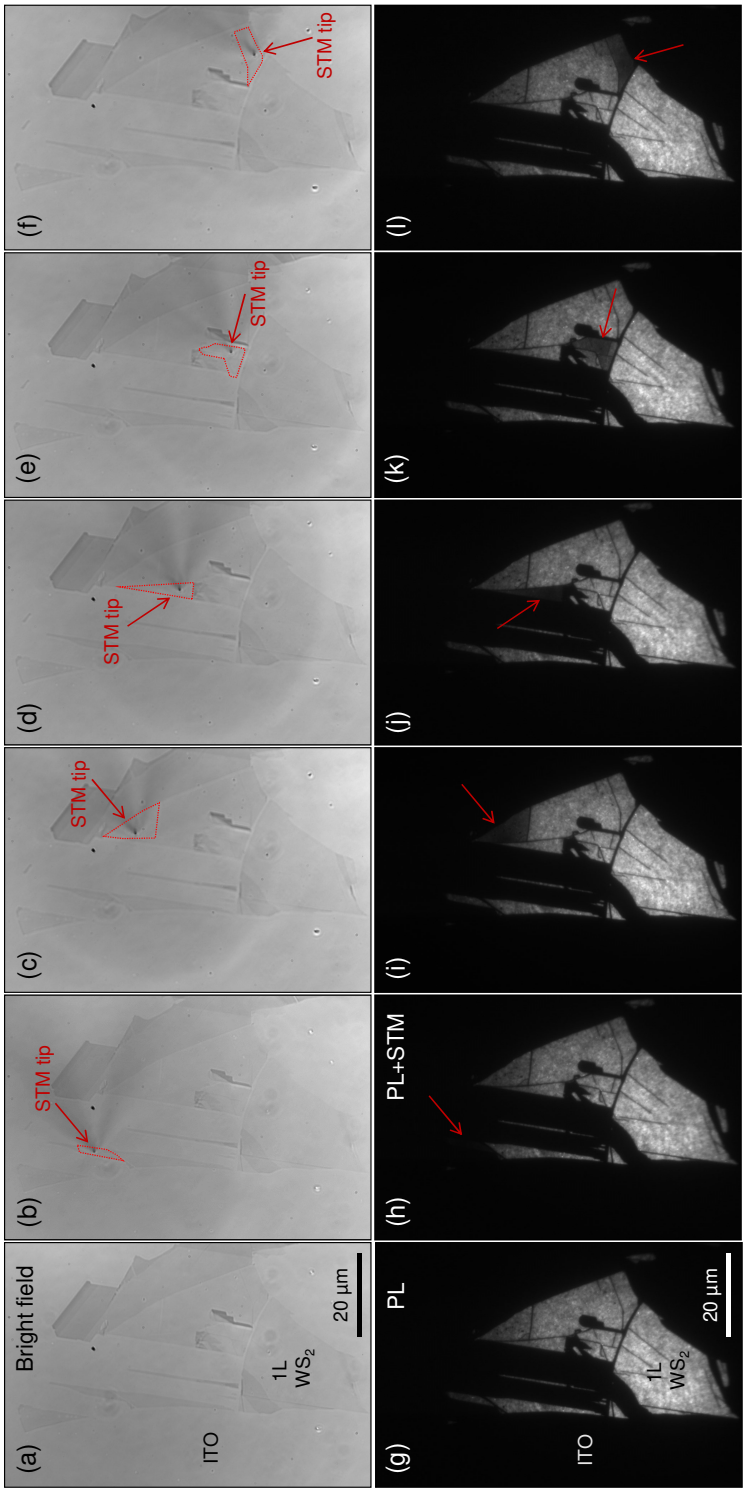

Figure S1: Extended data set used for Figure 1 of the letter (part 1). [(a)-(f)] Bright-field (white-light transmission) microscopy images and [(g)-(l)] wide-field laser-induced PL microscopy images of the same area of the sample (more details available in Sec. S1).

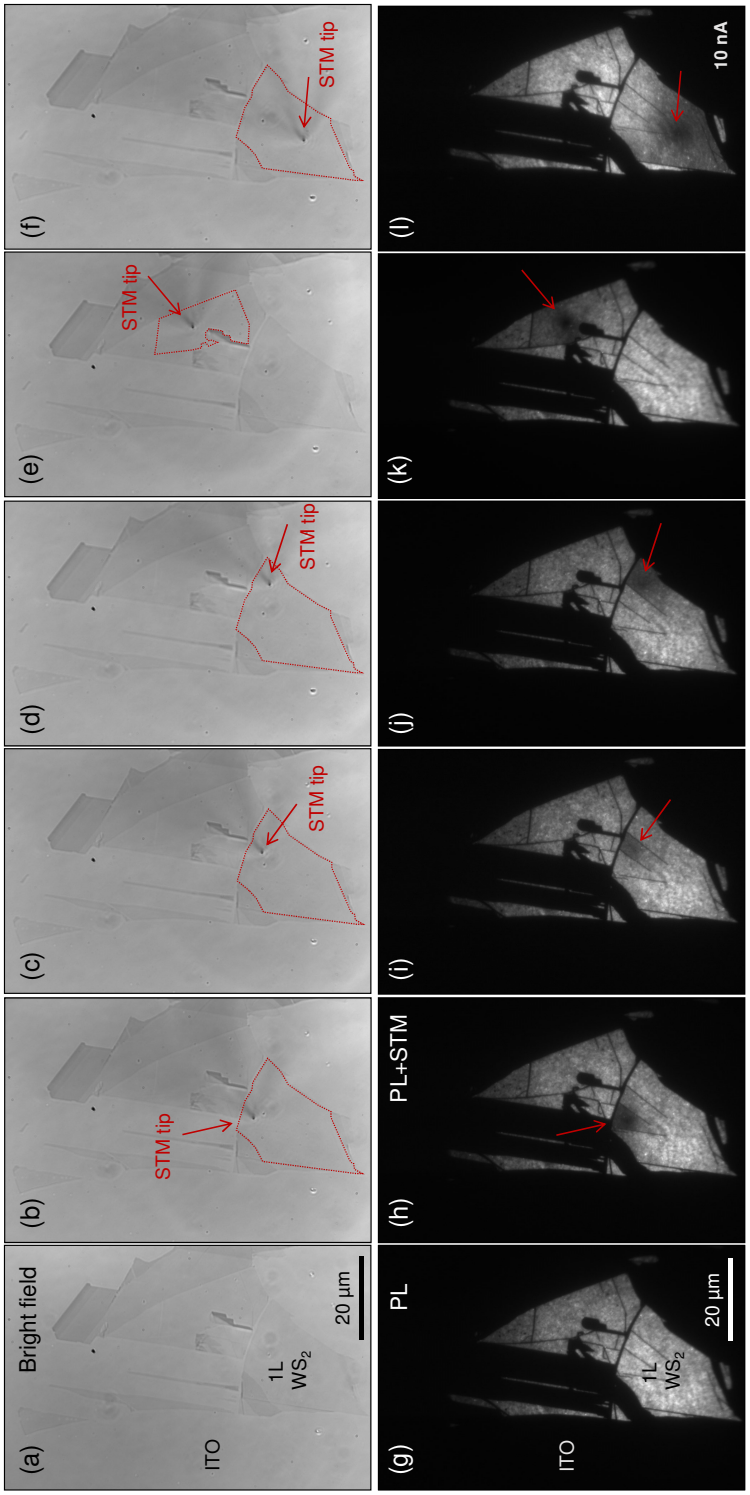

Figure S2: Extended data set used for Figure 1 of the letter (part 2). [(a)-(f)] Bright-field (white-light transmission) microscopy images and [(g)-(l)] wide-field laser-induced PL microscopy images of the same area of the sample (more details available in Sec. S1).

S2 Estimation of the PL quantum yield from Figure 1

Below, we detail how we estimate the PL quantum yield of our sample in absence of the STM tip. This is carried out using the PL image shown in Fig. 1(c) of the letter. We assume that the PL intensity is proportional to the radiative quantum yield and to the excitation power (linear excitation regime). The PL of the sample is excited using a collimated laser beam (excitation wavelength $\lambda_0 = 465.8$ nm, laser power 1 μW) in normal incidence through the substrate. Based on the diameter of the laser beam in the sample plane ($1/e^2$-width is about 120 μm) and the transmittance of the microscope objective at the laser wavelength (i.e., 0.75), we evaluate that the excitation power at the position of the flake, i.e., in the central part of the beam, is about 0.012 W cm^{-2}. This corresponds to an incident flux of 2.9 10^8 photons μm^{-2} s^{-1}. According to previous publications,[S1] the absorbance of monolayer WS_2 at the excitation wavelength is 0.06. From this data we estimate the number of absorbed photons per unit area and per unit time, N_{abs}. In the PL microscopy image, each pixel of the CCD camera covers an area of 7.5 $10^{-3}\mu$m^2 in the sample plane. Thus, we obtain $N_{abs} \approx 1.3\ 10^5$ photons s^{-1} per pixel, which we compare to the number of emitted photons per pixel in the PL image. In Fig. 1(c), after subtraction of the background, we measure on average 62 counts s^{-1} per pixel. In order to convert this count number into a number of photons emitted in the collection cone of the objective, we need to consider the following: the analog-to-digital conversion gain of the CCD camera (5.3 electron count^{-1}), the quantum efficiency of the CCD camera (0.80 at $\lambda_0 = 610$ nm), the transmittance of the microscope objective (0.82 at $\lambda_0 = 610$ nm) and that of the lenses used to form the real-space image on the CCD camera (0.90 for the set of four lenses). If the emitting dipole is oriented parallel to the surface of the ITO-coated glass substrate, 61% of its radiation is emitted in the substrate.[S2] Assuming that our objective lens collects all the light emitted in the substrate, we obtain a value of about 9.2 10^2 s^{-1} per pixel for the number of photons N_{PL} emitted in all directions of space. Finally, the PL quantum yield is estimated from the ratio of N_{PL} to N_{abs}. Using this procedure, the PL quantum yield is found to approximately equal 0.007.

We assume that the first source of uncertainties in our estimation of the PL quantum yield is the determination of the excitation power at the position of the flake, due to the spatial inhomogeneity of the laser intensity in the illuminated area. Thus, we estimate that the error in the determination of the PL quantum yield is about ±40%, i.e., the PL quantum yield equals 0.007 ± 0.003.

S3 Quantitative analysis of PL quenching (Figure 1)

In this section, we provide a quantitative analysis of the quenching effect observed in the PL microscopy images shown in Fig. 1 in the letter. Figures S3(a) to S3(f) shows false-color images that are obtained by dividing the PL images shown in Fig. 1(d) to 1(i) (where the STM tip is engaged) by the PL image shown in Fig. 1(c) (where the STM tip is far away from the sample), respectively. Beforehand, the noise background is subtracted from the PL images. They are also normalized by the excitation power. Consequently, the resulting images in Fig. S3 reveal the variation of the PL quantum yield, Q/Q_0, where Q and Q_0 are the PL quantum yield of the sample with and without the quenching effect due to the biased tip-sample junction and tunneling current, respectively. In Sec. S2, we estimated that the average value for Q_0, $\bar{Q_0} = 0.007 \pm 0.003$. The text in the images of Fig. S3 indicates the area S of the flake domain that is targeted by the STM tip and the variation of the PL quantum yield Q/Q_0 averaged over this area. (Note that S is the same for Figs. S3(c) to S3(f).) We observe that the most significant reduction of the PL quantum yield averaged over S occurs for the smallest area of the flake domain (S); this naturally results from the fact that the quenching effect has a limited lateral extent and decreases with the lateral distance from the STM tip. For all images, the sample bias is $V_s = 1.5$ V and the current setpoint is $I_t = 1$ nA, except for Fig. S3(f), where $I_t = 10$ nA. This analysis confirms that the quenching effect increases with the tunneling current.

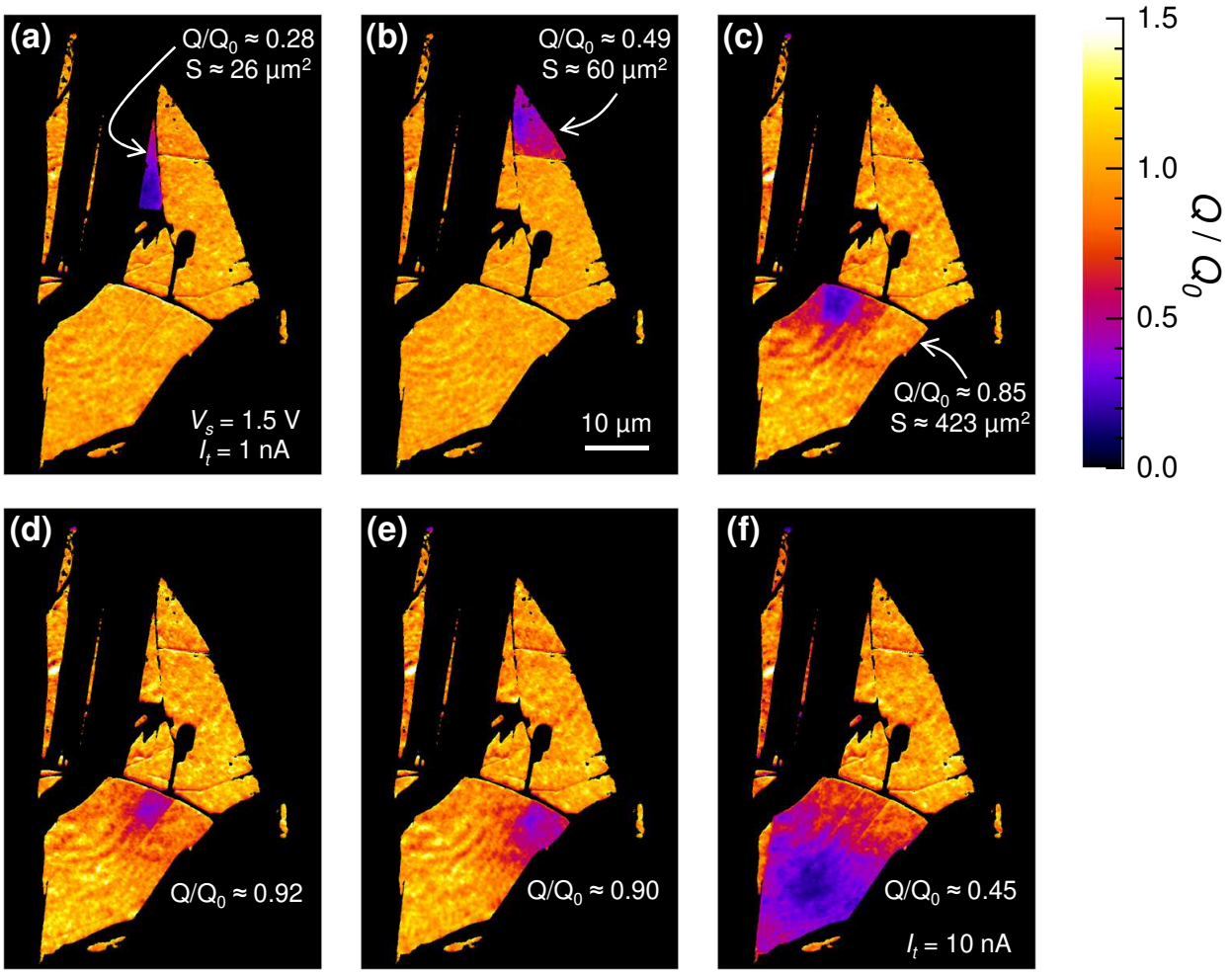

Figure S3: False-color images of PL quantum yield variations induced by the STM. These images are obtained by dividing the PL microscopy images shown in Fig. 1(d) to 1(i) in the letter (STM tip engaged) by the PL image shown in Fig. 1(c) (STM tip withdrawn), respectively. (More details are available in Sec. S3).

S4 Estimation of the charge carrier density

In this section, we introduce a simple approach to estimate the charge carrier density in the monolayer WS_2 flake under the STM tip. This charge carrier density is induced by the presence of the biased tip-sample junction and the tunneling current. Figure S4 shows a simplified schematics of the sample and experiment, as well as a circuit diagram and an energy diagram of the biased tip-sample junction. As mentioned in the letter, a partial electronic decoupling of the WS_2 flake and the conducting substrate is very likely due to the presence of a nanometer-thin layer of adsorbed water that is inherent to experiments in ambient conditions.[S3,S4] The presence of a thin insulating layer between the monolayer WS_2 flake and the ITO-coated glass substrate may induce a voltage drop between the flake and the substrate, by a fraction α of the bias voltage V_s applied to the tip-sample junction. Here, we assume that the voltage drop in the water layer is lower than the minimum voltage to start water electrolysis, so that water can effectively be considered as insulating. Below, we model the flake-substrate junction as a simple parallel-plate capacitor, as shown in Fig. S4(d), and we thus estimate the density of charge carriers stored in the capacitor. Within this model, the bias voltage applied between the plates of the capacitor is $U = \alpha V_s$. In principle, α may be determined through STM spectroscopy (STS) measurements; however, STS in air is hampered by a lack of sufficient thermal and mechanical stability on the subnanometer scale during the time required for such measurements. Therefore, we estimate α from luminescence experiments, as explained below.

In the present study, we assume that "long-range" PL quenching is observed only when the Fermi level of the STM tip is above the conduction band minimum (CBM) of monolayer WS_2; thus, the CBM energy with respect to the Fermi level in the substrate may be determined from the minimum bias voltage V_s^+ necessary to observe "long-range" PL quenching. From Fig. 2(g) in the letter, we infer that $V_s^+ \approx 1.1$ V for a current setpoint $I_t^+ = 3$ nA. In a previous study,[S5] we measured the STM-induced luminescence (STML) of similar WS_2/ITO samples and determined that STML may be observed at a negative sample bias, provided that

the Fermi level of the STM tip is below the valence band maximum (VBM) of monolayer WS_2; thus, the VBM energy with respect to the Fermi level in the substrate may be determined from the negative bias voltage V_s^- corresponding to the STML onset. For $I_t^- = 10$ nA, we measured $V_s^- \approx -1.8$ V.[S5] Similarly as for STS measurements, the apparent electronic bandgap energy $e(V_s^+ - V_s^-) = 2.9$ eV measured in this way is larger than the actual electronic bandgap energy E_g of monolayer WS_2 reported in the literature, e.g., $E_g = 2.41 \pm 0.04$ eV,[S6] due to the voltage drop between the substrate and the flake (see Fig. S4(c)).

In order to determine α, we model the tip-sample "double" junction as two resistances connected in series. As shown in Fig. S4(b), ρ and R are the electrical resistances of the tip-flake and flake-substrate junctions, respectively. V_s is the bias voltage applied to the tip-sample junction and I_t is the tunneling current. We assume that R is independent of V_s and I_t, i.e., Ohm's law can be applied to the flake-substrate junction. Applying Kirchhoff's voltage law in this circuit, we obtain $\alpha = \dfrac{R}{\rho + R} = \dfrac{I_t}{V_s} R$ and the difference between the apparent and actual electronic bandgap energy reads $e(V_s^+ - V_s^-) - E_g = eR(I_t^+ + I_t^-)$. Thus, we find $R \approx 3.8\ 10^7\ \Omega$. Using this value, we can obtain α for any V_s and I_t. In Fig. 1 in the letter, $V_s = 1.5$ V and $I_t = 1$ nA, i.e., $\alpha \approx 0.025$, except in Fig. 1(i), where $I_t = 10$ nA, i.e., $\alpha \approx 0.25$. This is an approximation of the voltage drop between the flake and substrate under the tip, at the position of the tunnel current, i.e., where the voltage drop is the highest; however, this voltage drop is expected to decrease with the lateral distance from the tip. Below, we use this estimation of α to determine the charge carrier density induced by the STM just below the tip, where this density is expected to be the highest.

The flake-substrate junction is modeled as a simple parallel-plate capacitor, as shown in Fig. S4(d). The spacing between the plates, d, corresponds to the effective thickness of the thin insulating layer between WS_2 and ITO. Based on previous STM measurements,[S4] we estimate that $d \approx 1.5$ nm. We consider that the material between the plates is water, whose static dielectric permittivity is $\varepsilon \approx 80\varepsilon_0 \approx 7\ 10^{-10}$ C V^{-1} m^{-1}. The bias voltage applied between the two plates is $U = \alpha V_s$. The charge density on the plates is $\sigma = \dfrac{\varepsilon U}{d}$. In Fig. 1 in

the letter, $\alpha V_s \approx 0.038$ V, i.e., $\sigma \approx 0.018$ C m$^{-1} \approx 1.1\ 10^{13}$ electrons cm^{-2}, except in Fig. 1(i), where $\alpha V_s \approx 0.38$ V, i.e., $\sigma \approx 0.18$ C m$^{-1} \approx 1.1\ 10^{14}$ electrons cm^{-2}. Note that these are estimated values of the charge carrier density under the STM tip; however, the charge carrier density anywhere else in the flake should be proportional to the local voltage drop between the flake and substrate. This voltage drop decreases when the lateral distance from the tip increases. Moreover, there are several sources of uncertainties in our estimation of the charge carrier density under the STM tip. The first one may be the determination of the apparent electronic bandgap energy. In addition, different values of the actual electronic bandgap energy may be found in the literature, which depend on the method used to determine it and on the sample substrate or encapsulation. These reported values for E_g differ from each other by up to several hundreds of meV.[S6–S10] Thus, the model introduced above provides the order of magnitude of the charge carrier density under the STM tip.

As a final remark, in the experiment, electron tunneling and local electrostatic gating effects due to the presence of the biased tip-sample junction are two effects that may coexist within all the investigated bias voltage range. There is inevitably a tunneling current when the tip is engaged, since we use an STM in constant current mode. Unlike for a typically gated sample, we cannot create an electrostatic gating effect in absence of a tunneling current between the sample and the gate, i.e., the STM tip. Nevertheless, by varying the bias voltage, we can control the energy position of the Fermi level of the tip with respect to the conduction band minimum (CBM) of the TMD. When the Fermi level of the tip is above the CBM, electrons can tunnel into the conduction band of the WS_2 layer, leading to charging of the WS_2/ITO system, which then acts as a parallel-plate capacitor. Only in this case is the necessary doping level for the observation of long-range PL quenching attained.

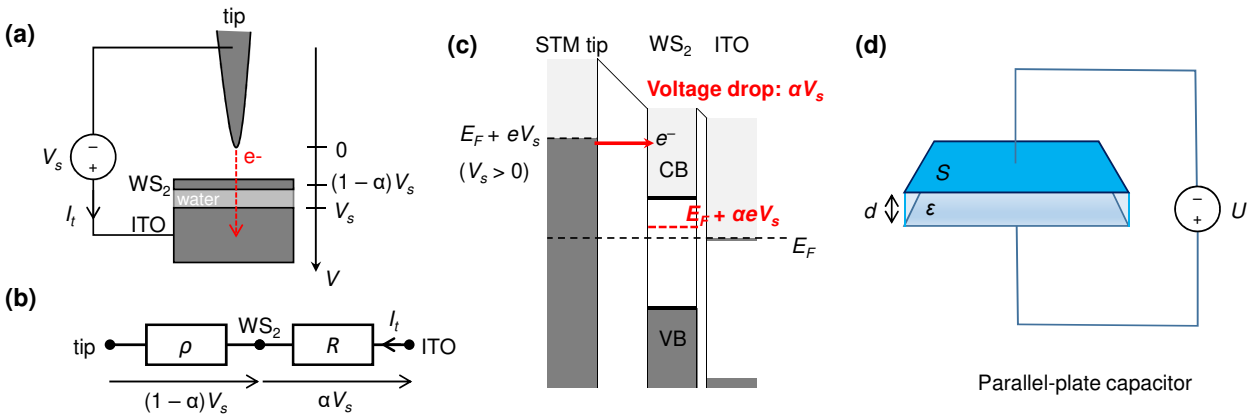

Figure S4: Simplified (a) schematic of the sample and experiment, (b) biased tunneling junction circuit diagram, and (c) biased tip-sample junction energy diagram. Here we consider the presence of a thin insulating layer (e.g., of adsorbed water) between the monolayer WS_2 flake and the ITO-coated glass substrate. This insulating layer induces a voltage drop between the flake and the substrate, which is a fraction α of the bias voltage V_s applied to the tip-sample junction. In (a), V and the vertical axis denote the electric potential with respect to the grounded tip. In (b), ρ and R are the electrical resistances of the tip-flake and flake-substrate junctions, respectively. I_t is the tunneling current, i.e., the electrical current flowing in the circuit. In (c), E_F, CB and VB refer to the Fermi level of the substrate, and the conduction and valence bands of WS_2, respectively. (d) Schematics of a parallel-plate capacitor, where S, d, ε and U are the plate area, the spacing between the plates, the static dielectric permittivity of the material between the plates and the bias voltage applied between the two plates, respectively (more details available in Sec. S4).

S5 Additional data on the PL bias voltage dependence for positive and negative polarities

Figures S5 and S6 show additional data which complement those shown in Figures 2 and 3 of the letter, which further reveal the bias voltage dependence of the STM-induced quenching of the PL at positive and negative bias polarities. In brief, a "long-range" quenching effect is only observed at positive sample bias. The onset of this quenching effect is observed at a bias voltage of about 1.0 V. Above this quenching onset voltage, the strength of the quenching increases with the bias voltage and tends to a value that may vary from one area of the flake to another. At negative sample bias, only a "short-range" quenching effect is observed. The strength of the quenching slightly increases with the absolute value of the bias voltage; however, it does not exhibit a clear onset voltage within the investigated voltage range, i.e., from -0.5 to -4 V. For both bias polarities, the STM-induced quenching of the PL is reversible. The PL recovery observed after the withdrawal of the STM tip apparently follows an exponential law, which is reminiscent of the discharging of a capacitor, with a time constant on the order of a few seconds or tens of seconds. The details of Figs. S5 and S6 may be found below.

In Figs. S5(a) to S5(e), a series of 175 PL microscopy images is recorded (at a rate of 1 frame s^{-1}) on a monolayer WS_2 microflake. While measuring the PL images, the STM tip is engaged and the sample bias is gradually increased from 0.5 to 1.5 V by steps of 0.1 V, before the tip is finally withdrawn. All the PL images of this series are divided by the image shown in Fig. S5(a), which is the first image of the series [i.e., $I(0)$]. Thus, the relative variation of the PL intensity (refered to as the "intensity ratio" in the following) is considered. A selection of intensity ratio images is shown in Figs. S5(b) to S5(d). These images are in false color and the intensity ratio is represented on a log scale and expressed in decibels (dB, $10 \log [I(t)/I(0)]$). The intensity ratio, averaged over a circular area of radius ≈ 1.0 μm centered on the position of the tip, is plotted in Fig. S5(e) versus time (t), together

with the applied (positive) sample bias. Figures S5(f) to S5(j) show similar data as those shown in Figs. S5(a) to S5(e), which have been measured under similar conditions but on a different area of the same flake. Figure S6 shows data obtained on the same flake using the same method, except that the applied sample bias is negative. In Figs. S6(a) to S6(e), the sample bias is gradually decreased from -1.5 to -4.0 V in steps of 0.1 V; whereas, in Figs. S6(f) to S6(i), the sample bias is increased from -3.0 to -0.5 V. In Figs. S6(d) and S6(i), the intensity ratio is averaged over a circular area of radius ≈ 0.4 μm centered on the position of the tip.

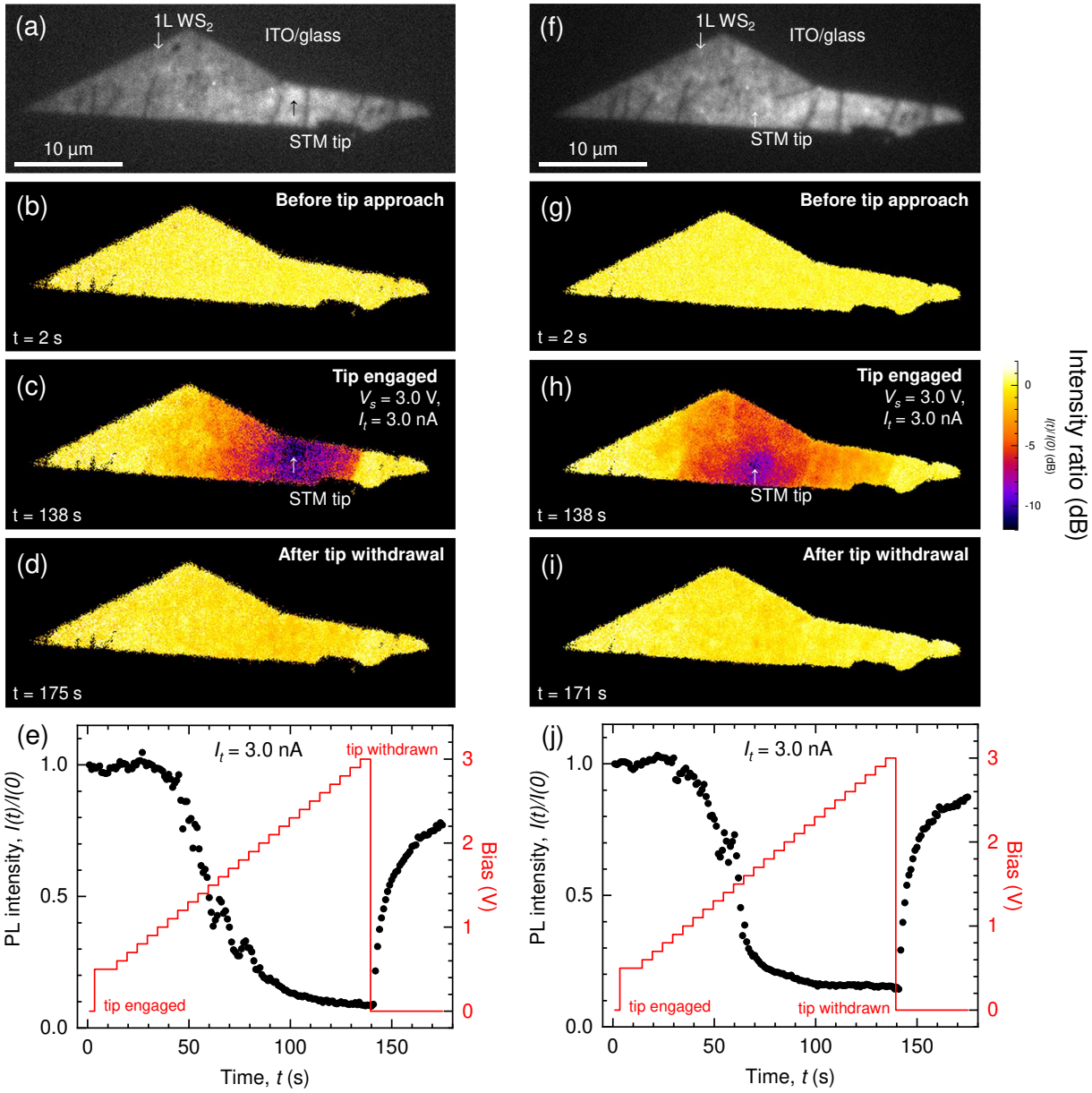

Figure S5: Additional data complementing that of Figure 2 of the letter (positive sample bias). [(a), (f)] Laser-induced PL microscopy images of a monolayer WS_2 microflake on ITO in the absence the STM tip. [(b)-(d) and (f)-(i)] PL intensity ratio, obtained by dividing the PL images by the image shown in (a) and (f), respectively (false colors, log scale from -12 to $+2$ dB). [(b), (g)]: before the approach of the STM tip; [(c), (h)]: with the STM tip in the tunneling regime, at sample bias $V_s = 3.0$ V and current setpoint $I_t = 3.0$ nA; [(d), (i)]: after tip withdrawal. [(e), (j)]: PL intensity ratio averaged over a 3.4 μm^2 area around the tip and STM bias voltage, plotted versus time (more details available in Sec. S5). In (c) and (h), the lateral position of the STM tip is designated by a white arrow.

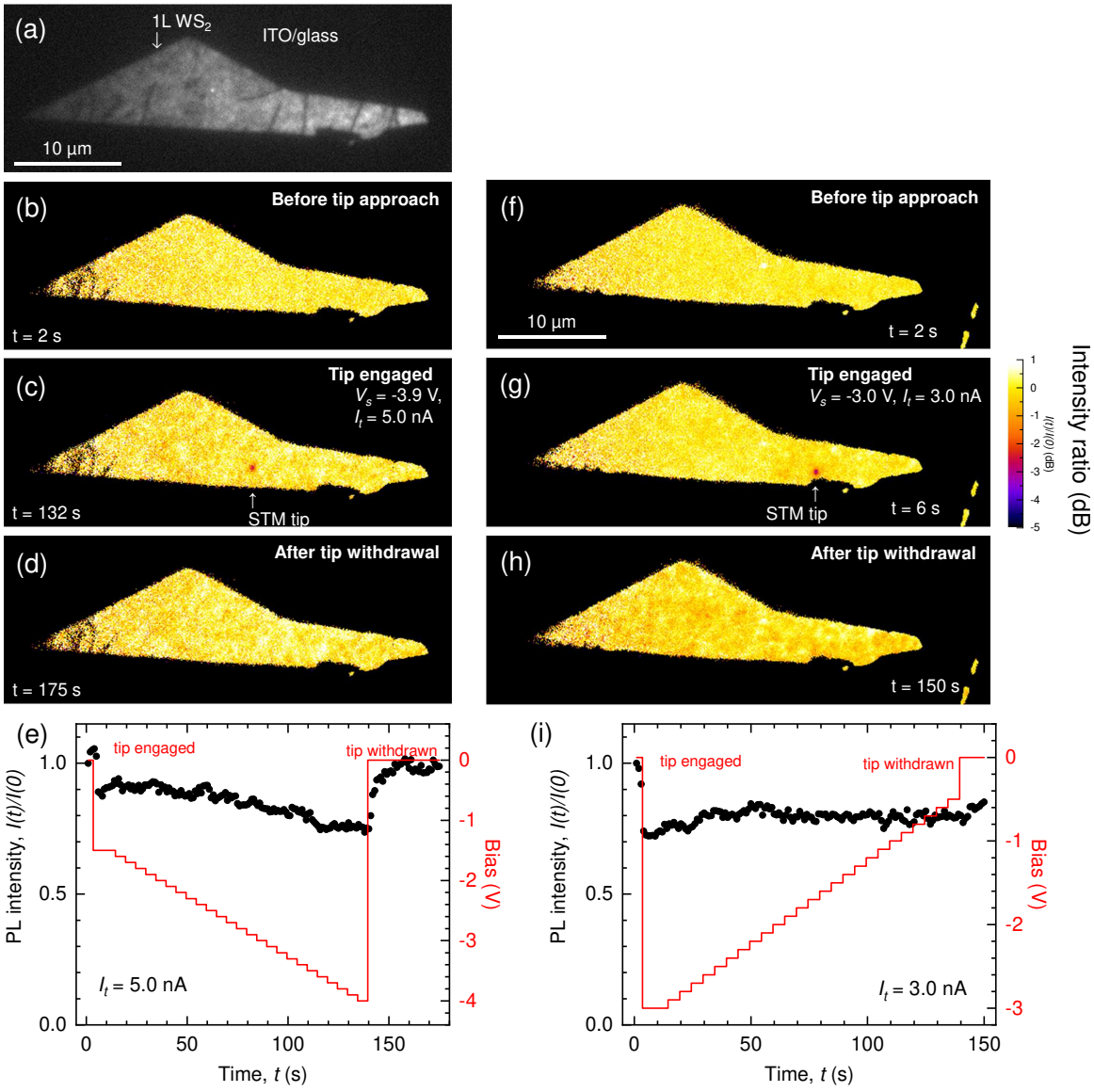

Figure S6: Additional data complementing that of Figure 3 of the letter (negative sample bias). (a) Laser-induced PL microscopy image of the same monolayer WS_2 microflake on ITO as in Fig. S5(a). [(b)-(d) and (f)-(h)] PL intensity ratio (false colors, log scale from -5 to $+1$ dB). [(b), (f)]: before the approach of the STM tip; [(c), (g)]: with the STM tip in the tunneling regime, at (c) $V_s = -3.9$ V / $I_t = 5.0$ nA and (g) $V_s = -3.0$ V / $I_t = 3.0$ nA; [(d), (h)]: after tip withdrawal. [(e), (i)]: PL intensity ratio averaged over a 0.6 μm^2 area around the tip and STM bias voltage, plotted versus time (more details available in Sec. S2). In (c) and (g), the lateral position of the STM tip corresponds to the center of the dark spot in the image.

S6 Simplified theoretical model of the non-radiative energy transfer from the excitons to the tungsten tip

Figure S7 shows the results of non-retarded electromagnetic calculations carried out within a simplified theoretical model of the exciton interaction with the STM tip. These results support our interpretation that the PL quenching effect observed in the almost diffraction-limited area under the STM tip, regardless of the bias voltage and at both bias polarities, is due to the near-field electromagnetic transfer of energy from the excitons to the tip, which primarily yields losses because of the non-plasmonic nature of the (tungsten) tip. As shown in Fig. S7(a), we model the STM tip as a tungsten sphere of radius 30 nm, which is a typical value for the radius of curvature of our STM tips.[S11] The spontaneous decay of the exciton is modeled as the emission of an oscillating electric dipole $\mathbf{p}$, which is located in a plane (xy) that is 1 nm away from the sphere (i.e., the vertical distance from the tip in the z direction is 1 nm). This electric dipole oscillates at the emission frequency of the bright exciton. The presence of the monolayer flake is not taken into account. The dipole $\mathbf{p}$ is oriented parallel to the axes x, y, or z, as defined in Fig. S7(a). In Fig. S7(b) (see dotted lines), the radiative decay rate Γ_r, normalized to that of the same dipole in free space $\Gamma_{r,0}$ (i.e., the Purcell factor), is plotted on a semilog scale as a function of the position of the dipole along the x-axis (i.e., lateral distance from the tip) for the x, y, and z-orientation of $\mathbf{p}$. On the same graph (see solid lines), we plot the sum of the radiative Γ_r and non-radiative Γ_{nr} decay rates, i.e., the total decay rate Γ, normalized to the radiative decay rate in free space. Here, we assume that the emission in free space, i.e., in absence of the tungsten sphere, is purely radiative (i.e., $\Gamma_0 = \Gamma_{r,0}$). Thus, the non-radiative decay rate in presence of the tungsten sphere, i.e. $\Gamma - \Gamma_r$, equals the rate of non-radiative energy transfer between the emitter and the tungsten sphere. As shown in Fig. S7(b), under the tip apex (i.e., at $x = 0$), the total decay rate Γ is increased by about four orders of magnitude, whereas the radiative decay rate

Γ_r either increases by one order of magnitude (for $\mathbf{p}_z$) or decreases by one to two orders of magnitude (for $\mathbf{p}_x$ and $\mathbf{p}_y$). Thus, the non-radiative energy transfer between the emitter and the tungsten sphere opens up new decay channels, which are almost entirely non-radiative. In Fig. S7(c), we only consider the average emission from $\mathbf{p}_x$ and $\mathbf{p}_y$, in order to simulate the emission of spin-allowed bright excitons, whose transition dipole moments are parallel to the (xy) plane.[S2] Several vertical distances to the sphere are considered. In the experiments, when the STM tip is in the tunneling regime, the tip-sample gap distance may vary between 0.5 to 2.0 nm, typically. Within this vertical distance range, the total decay rate under the tip apex (i.e., at $x = 0$) is increased by three to five orders of magnitude as compared to free space. According to Fig. S7(c), the tip effect on the total decay rate is mostly limited to an area corresponding to lateral distances of less than 60 nm. Below, we use the theoretical results shown in Figs. S7(b) and S7(c) to simulate the effect of this non-radiative energy transfer to the STM tip on the radiative quantum yield of the WS_2 monolayer. To obtain the results shown in Figs. S7(d) and S7(e), we consider that the radiative quantum yield of the emitter in absence of the tip is 0.007, as estimated from the experimental PL images shown in Fig. 1 (see calculation in Sec. S2). The variation of the radiative quantum yield is directly related to the variation of the PL intensity measured in the experiments, because PL intensity varies linearly with the radiative quantum yield, in the linear excitation regime. From Fig. S7(e), we infer that non-radiative energy transfer to the STM tip quenches the PL of the WS_2 monolayer under the tip and that this effect becomes negligible at lateral distances that are further than about 30 nm from the tip, i.e., distances that are small as compared to the diffraction limit of light and the spatial resolution of the optical microscope.

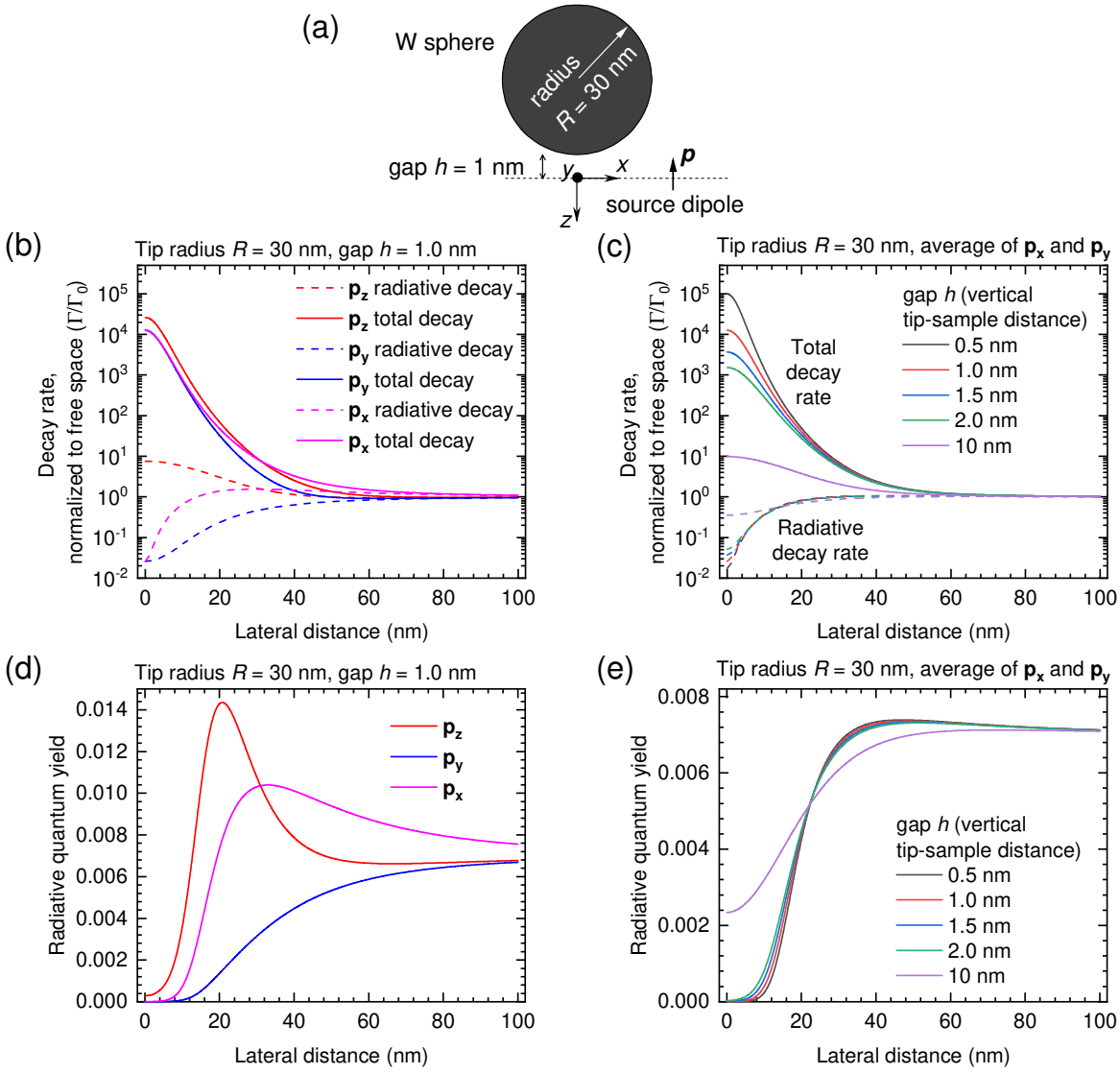

Figure S7: Simple model of the exciton interaction with the STM tip. (a) Schematics of the model: The exciton is modeled as a point-like oscillating electric dipole and the tip is considered to be a tungsten nanosphere. (b,c) The decay rate of the dipole, normalized to that in free space, is plotted as a function of its position along the x-axis (i.e., its lateral distance from the tip). (d,e) The radiative quantum yield of the dipole is plotted versus its lateral distance from the tip. We consider that the radiative quantum yield in free space is 0.007. More details available in Sec. S6.

S7 Evidence that STM-induced luminescence does not play a role

Figure S8 shows additional data which compliments that of Figure 4 of the letter. The results of Fig. S8 show that the STM-induced modifications of the PL spectra reported in Fig. 4(a) are not due to the STM-induced luminescence of monolayer WS_2.

In brief, Figure 4 of the letter shows that the PL spectrum of monolayer WS_2 features a peak at the exciton energy and a secondary contribution at the trion energy. When the STM tip is engaged, we observe that the intensity ratio of this secondary contribution versus the total emitted light increases by a factor of about 2 at positive sample bias, whereas it remains almost unchanged at negative bias. These observations remain true within the investigated bias voltage range, i.e., from 1.5 to 3.0 V in absolute value. This result is not consistent with the participation of electroluminescence, because STM-induced (electro)luminescence of monolayer WS_2 may be observed at both bias polarities and its onset is at a bias voltage of about 1.8 to 2.0 V at positive sample bias.[S5] Moreover, the quantum yield of STM-induced luminescence of monolayer WS_2 is about one order of magnitude higher at a sample bias of 3 V as compared to that at 2 V.[S5] Such a difference would also be observed in the intensity ratio of the excitonic and trionic contributions shown in Fig. 4(c) if the STM-induced modifications of the PL spectra reported in Fig. 4(a) were due to STM-induced luminescence of monolayer WS_2.

Furthermore, the additional data shown in Figure S8 reveals that the STM-induced modifications of the PL spectra measured in an area around the tip are highly similar to those measured in an area that is about 3 μm away from the tip. Again, such an observation is not consistent with a contribution from electroluminescence, because the STM-induced luminescence of monolayer WS_2 is localized in an almost diffraction-limited area around the lateral tip position.[S5] More details about Fig. S8 are given below.

Figure S8(a) is a PL microscopy image (in false colors) of the same flake as that shown in

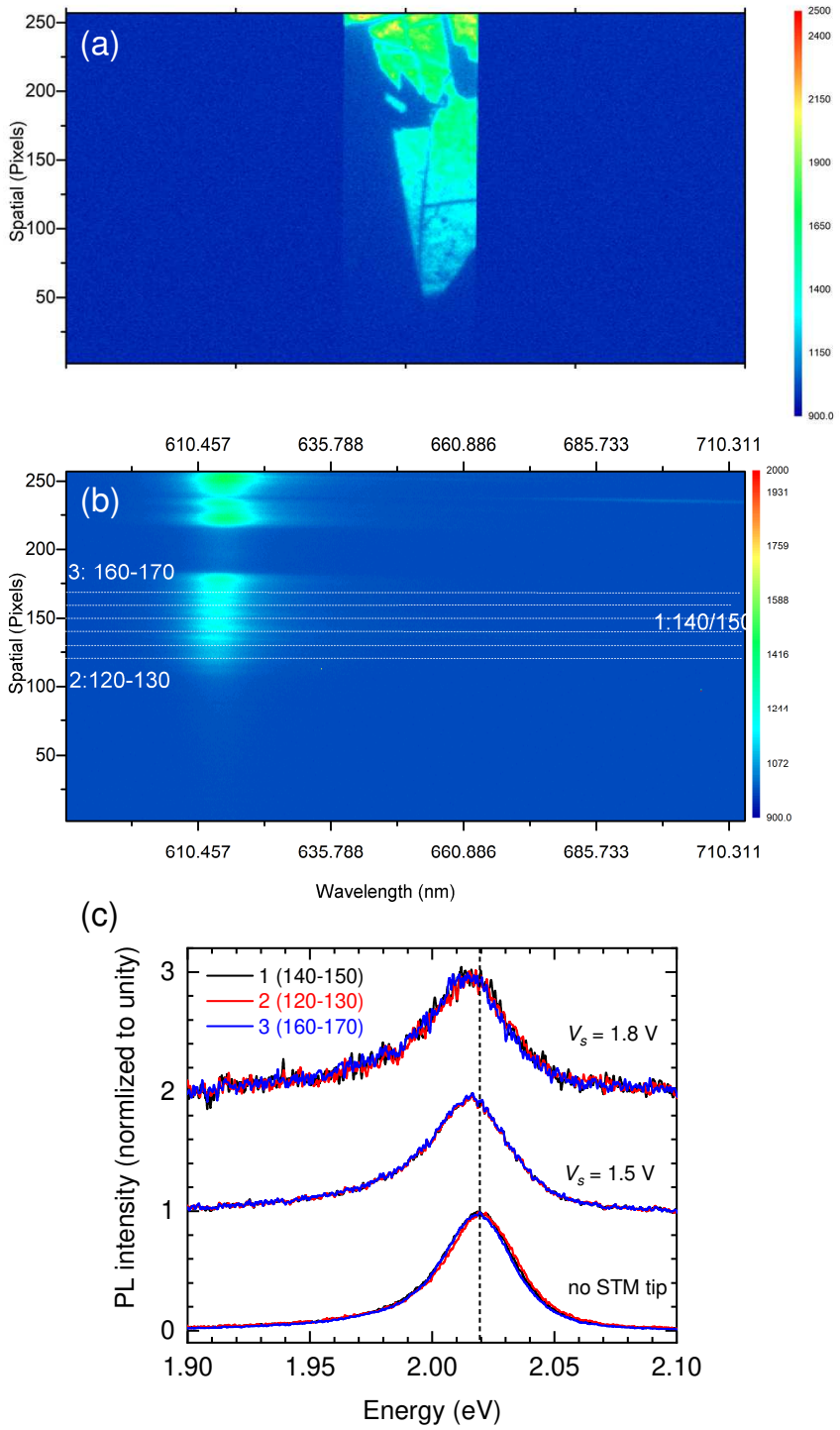

Figure S8: (a) False-color PL microscopy image of the same flake as that shown in Figure 1 of the letter, measured through the wide-opened entrance slit of the spectrometer. (b) Spectrally dispersed image of the PL measured through the 50 μm-wide entrance slit of the spectrometer in the same area of the sample. (c) PL spectra measured by summing the lines 140 to 150, 120 to 130, and 160 to 170 of the CCD sensor, as shown in panel b, respectively. More details available in Sec. S7.

Figure 1 (the image appears vertically flipped), which is the raw image file that is captured by the CCD sensor coupled to the optical spectrometer, when the entrance slit is completely opened (slit width equals 2 mm) and the zeroth order of the diffraction grating is considered. Here, the STM tip is withdrawn far from the sample. Figure S8(b) is the image that is captured when the entrance slit is closed down to a width of 50 μm and the first order of the grating is used; i.e., it is a spectrally resolved PL intensity profile along a vertical line crossing the sample area shown in Fig. S8(a). Three horizontal areas are delineated (white lines) in Fig. S8(b), which correspond to lines 140 to 150, 120 to 130, and 160 to 170 of the CCD sensor. Thus, we detect the light emitted from areas that are defined by the height (i.e., 10 lines) of each band and the slit width (i.e., 50 μm), which correspond to about 1.7 μm and 0.33 μm in the sample plane, respectively. In order that STM-induced electroluminescence of the sample is undetected or negligible as compared to the detected PL signal, we slightly shift the lateral position of the STM tip by a few pixels out of the area selected by the entrance slit of the spectrometer. In this way, STM-induced electroluminescence may be avoided, even at bias voltages exceeding the electroluminescence onset voltage.

S8 Effect of alternating positive and negative sample bias

In Figure S9, we examine the effect of alternating positive and negative sample bias. We use the entrance slit of an imaging spectrometer to select the PL emitted from a narrow, micrometer-long band about the tip position. Figure S9(a) shows (in chronological order from bottom to top) a series of PL spectra measured in the same area at various bias voltages of different sign and of different values. We successively measure the PL spectrum with the tip engaged or withdrawn, i.e., in the tunnel regime with the feedback loop closed or with the tip retracted micrometers away from the sample. We alternate positive and negative sample bias and increase the bias voltage after each sequence. The lateral position of the STM tip on the sample is the same for all measurements up to the experimental precision (i.e., neglecting mechanical drift). The data shown in Fig. S9(a) qualitatively confirms the effect observed in Figs. 1 to 3 in the letter, i.e., PL is strongly quenched at positive sample bias, but not at negative sample bias when the PL intensity is averaged over a micrometer-scale area around the tip. In Fig. S9(b), we study the variation of the integrated PL throughout the sequence of STM-induced modifications described above, which unfolds chronologically from left to right. Sample bias is given in the top part of the figure. The integrated PL is retrieved from the PL spectra by integrating the area under the curve over energy. We find that the relative variation of the integrated PL *with respect to its initial value* before any STM manipulation ranges from 0.05 (at 1.8 V) to 1.25 (at -2.8 V). Nevertheless, a clear voltage-dependence of the quenching factor at positive sample bias is difficult to obtain from Fig. S9(b), possibly due to the inertia of the PL recovery after tip withdrawal. In order to avoid such artifacts, we now reconsider the same data but *with respect to the result obtained just beforehand in the previous step* where the tip is withdrawn. In Fig. S9(c), we plot the relative variation of the integrated PL when the STM tip is engaged, as compared to what is measured in the step just before, where the tip is withdrawn. Thus, we find that the PL

is quenched by a factor of 4 to 10 at positive sample bias within the investigated voltage range, with a general tendency of this factor to increase with voltage. At negative sample bias, we obtain relative variations greater than one (except at -3 V), which indicates that the PL recovery after quenching at positive sample bias may be improved by reversing the bias polarity of the tip-sample junction. This observation is consistent with a quenching effect due to electron tunneling-induced doping of the semiconductor, since reversing the bias polarity of the STM junction may contribute to the discharging of the flake or may compensate for the native n-doping of monolayer WS_2.

The PL spectra shown in Fig. 4 in the letter are taken from the same data set as that used in Fig. S9, except that in Fig. 4 the intensity of the PL spectra is normalized to unity.

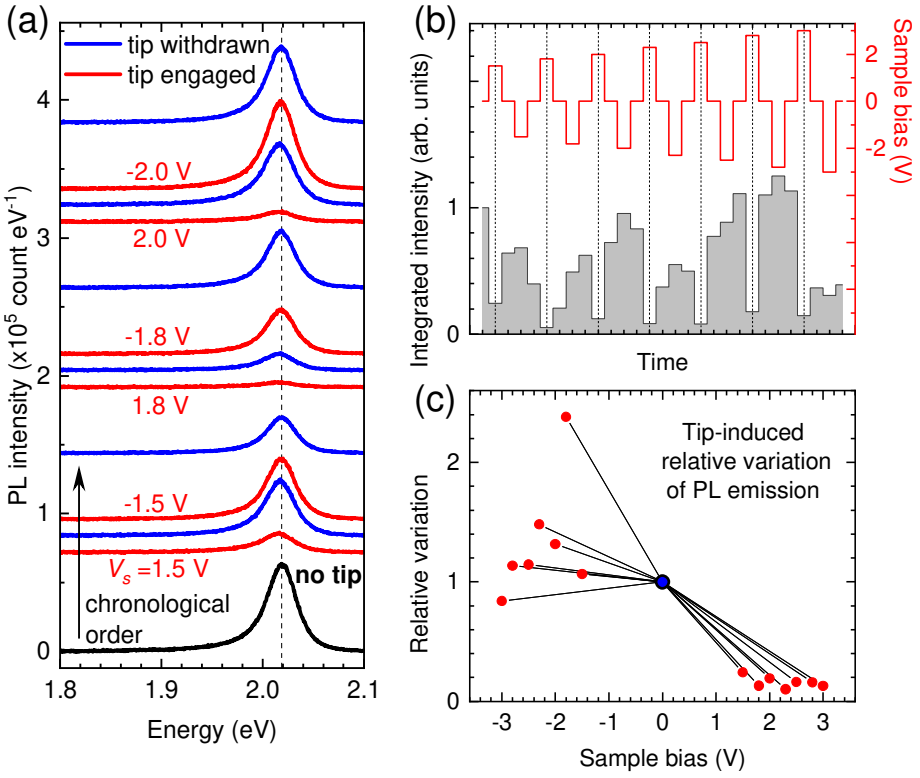

Figure S9: Spectral PL distribution and bias-dependence of the STM-induced effect. (a) PL spectra of monolayer WS_2 measured in the same area of the sample in a sequence where the STM tip is either withdrawn (blue curves) or engaged (red curves), at various sample biases. Chronological order is from bottom to top, and the first spectrum (black curve labeled "no tip") is measured with the tip withdrawn before any STM manipulation of the area. Setpoint current is 3 nA in all the measurements involving the STM. PL: laser excitation at $\lambda = 465.8$ nm, longpass filter from $\lambda = 491$ nm. (b) Integrated area under the curve of the PL spectra (grey bars) and bias voltage (red line) in the same chronological order as in (a) (from left to right). (c) Relative variation of the integrated PL when the STM tip is engaged, as compared to the measurement just before, when the tip was withdrawn (see Figure S10 for more details).

Figure S10 provides graphical help to understand how Fig. S9(c) is obtained. The area under the curve of the PL spectra is integrated over energy. In Fig. S10, the black dot corresponds to the spectrum measured before any STM manipulation, whereas the red and blue dots correspond to those measured when the tip is engaged and when it is withdrawn, respectively. In order to obtain the graph shown in Fig. S10(b) from that shown in Fig. S10(a), we divide the value corresponding to each red dot by that corresponding to the blue dot just before in the chronological order of the sequence of measurements.

Finally, Fig. S9 above and Fig. 4 in the letter show that no significant modification of the PL spectrum is measured when the STM tip is engaged for a negative sample bias of -1.5 V, as compared to when the tip is withdrawn several micrometers away from the sample. The modification of the PL spectrum is observed only for positive sample biases. This shows that the modification of the PL spectrum does not result from far-field interference effects due to the presence of the tip, since such effects are not expected to depend on the bias polarity.

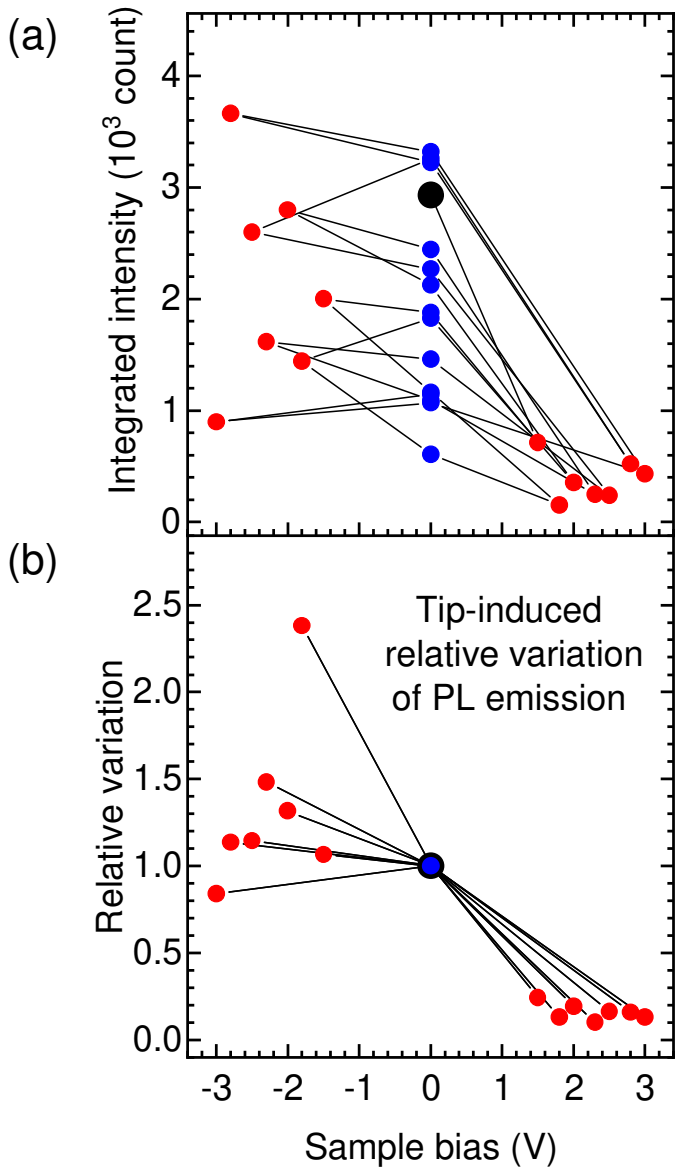

Figure S10: Graphical help to understand how Fig. S9(c) is obtained. More details available in Sec. S8.

S9 Does "ionic gating" play a role?

Given that all the discussed experiments are carried out in air, the question naturally arises as to whether "ionic gating" may play a role in the long-range PL quenching effect reported in this letter. Here, "ionic gating" means that a layer of water adsorbed on top of the TMD monolayer or bridging the tip-sample junction acts as a microscale electrode due to the formation of an electrical double layer, via migration of the ions in this water layer.[S12] However, though a molecular layer of water can often adsorb on a sample exposed to laboratory air,[S13] we show below that the hypothesis that ionic gating significantly contributes to the long-range PL quenching effect can be ruled out. This is based on experimental observations and simple reasoning about the principle of STM.

The experiments reported in this letter are based on the use of an STM operated in constant current mode. In such a technique, the presence of a tunneling current between the tip and the sample is required. In order that a tunneling current flows through the tip-sample junction, an insulating medium must separate the tip from the sample, and the tip-sample junction must be electrically biased. In other words, the presence of a static electric field in the junction is a prerequisite to the existence of a tunneling current. If a conductive layer bridged the tip-sample gap, the tunneling junction would be short-circuited. In such a case, the current flowing through the tip-sample junction would not decay exponentially with the tip-sample distance; thus, the STM feedback loop would actuate the retraction of the tip. Such behavior, however, is not observed experimentally.

Moreover, if a water bridge fills the gap between the tip and sample, we would not be able to carry out stable STM measurements in constant current mode at bias voltages exceeding the electrolysis potential of water (in theory 1.23 V, in practice 1.5 to 2.0 V). Indeed, at such bias voltages, the ionic current would dominate over the tunneling current and the tip-sample distance controlled by the STM feedback loop would become highly unstable. Such bias-dependent instabilities were observed on rough surfaces, such as thermally evaporated gold films.[S3] However, we do not experimentally observe such instabilities on monolayer TMDs.

Figure S11 shows histograms of the measured STM current recorded during the measurement of the data shown in Fig. S5. These histograms show that the statistical distribution of the tunneling current around the current setpoint is consistent with stable STM operation in constant current mode in ambient conditions, regardless as to whether the bias voltage is lower (1 V) or higher (3 V) than the electrolysis potential of water. Based on this result, we rule out the presence of a water bridge between the STM tip and the TMD monolayer.

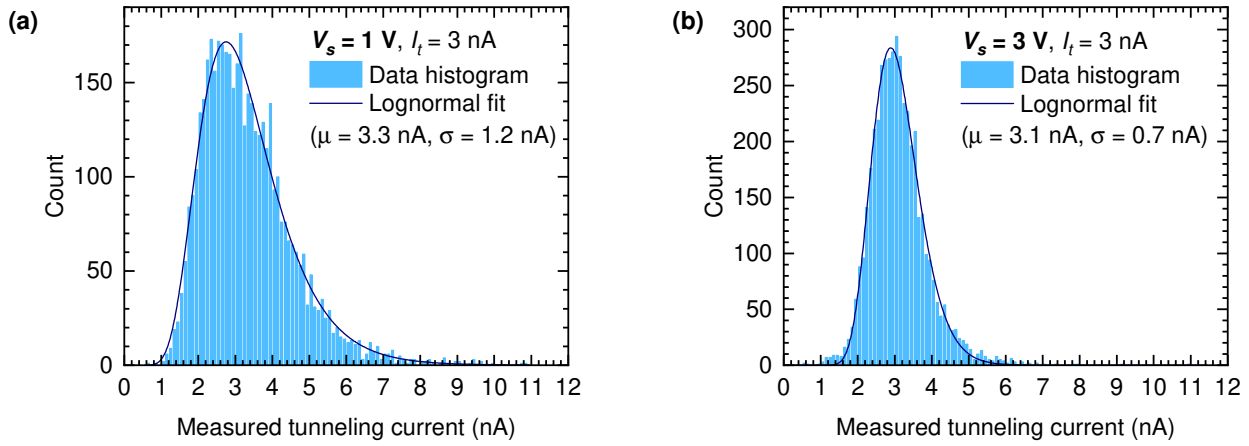

Figure S11: Histograms of the measured STM current recorded during the measurement of the data shown in Figs. S5(c) and S5(e). In both measurements shown here, the sample bias is positive and the setpoint current is 3 nA. In (a) and (b), the bias voltage is 1 V and 3 V, i.e., lower and higher than the theoretical hydrolysis potential of water (i.e., 1.23 V), respectively. The histograms are fit using a lognormal law with parameters μ (mean) and σ (standard deviation). More details available in Sec. S9.

As shown in Fig. S11, a lognormal law fits the statistical distribution of the measured STM current very well. Such good agreement is expected in stable STM operation in constant current mode, because the tunneling current decays exponentially with the tip-sample distance. The tip-sample distance may slightly fluctuate around its mean value, due to external perturbations that are inherent to operation in air. In a first approximation, these are random fluctuations; thus, their statistical distribution follows a normal law. As a result, a lognormal distribution is observed for the tunneling current. Moreover, we find a lower standard deviation for the current distribution measured at 3 V as compared to 1 V. We assume that this is because the tip-sample distance at a given current setpoint increases

with the applied bias voltage. Due to the exponential dependence of the current on the tip-sample distance, the same distance fluctuations yield lower current fluctuations when the bias voltage is higher. Such a result would not be observed if a water bridge spanned the tip-sample junction, because STM current fluctuations would strongly increase when the bias voltage is higher than the hydrolysis potential of water, due to the onset of an ionic current, which would not decay exponentially with the tip-sample distance.[S3] Therefore, we believe that ionic gating cannot explain our experimental observations.

References

[S1] Li, Y.; Chernikov, A.; Zhang, X.; Rigosi, A.; Hill, H. M.; van der Zande, A. M.; Chenet, D. A.; Shih, E.-M.; Hone, J.; Heinz, T. F. Measurement of the optical dielectric function of monolayer transition-metal dichalcogenides: MoS_2, $MoSe_2$, WS_2, and WSe_2. *Phys. Rev. B* **2014**, *90*, 205422.

[S2] Pommier, D.; Bretel, R.; Parra López, L. E.; Fabre, F.; Mayne, A.; Boer-Duchemin, E.; Dujardin, G.; Schull, G.; Berciaud, S.; Le Moal, E. Scanning Tunneling Microscope-Induced Excitonic Luminescence of a Two-Dimensional Semiconductor. *Phys. Rev. Lett.* **2019**, *123*, 027402.

[S3] Rogez, B.; Cao, S.; Dujardin, G.; Comtet, G.; Le Moal, E.; Mayne, A.; Boer-Duchemin, E. The mechanism of light emission from a scanning tunnelling microscope operating in air. *Nanotechnology* **2016**, *27*, 465201.

[S4] Peña Román, R. J.; Auad, Y.; Grasso, L.; Alvarez, F.; Barcelos, I. D.; Zagonel, L. F. Tunneling-current-induced local excitonic luminescence in p-doped WSe_2 monolayers. *Nanoscale* **2020**, *12*, 13460–13470.

[S5] Peña Román, R. J.; Pommier, D.; Bretel, R.; Parra López, L. E.; Lorchat, E.; Chaste, J.; Ouerghi, A.; Le Moal, S.; Boer-Duchemin, E.; Dujardin, G.; Borisov, A. G.; Zagonel, L. F.; Schull, G.; Berciaud, S.; Le Moal, E. Electroluminescence of monolayer WS_2 in a scanning tunneling microscope: Effect of bias polarity on spectral and angular distribution of emitted light. *Phys. Rev. B* **2022**, *106*, 085419.

[S6] Chernikov, A.; Berkelbach, T. C.; Hill, H. M.; Rigosi, A.; Li, Y.; Aslan, O. B.; Reichman, D. R.; Hybertsen, M. S.; Heinz, T. F. Exciton Binding Energy and Nonhydrogenic Rydberg Series in Monolayer WS_2. *Phys. Rev. Lett.* **2014**, *113*, 076802.

[S7] Zhu, B.; Chen, X.; Cui, X. Exciton Binding Energy of Monolayer WS_2. *Sci. Rep.* **2015**, *5*, 9218.

[S8] Schulman, D. S.; Arnold, A. J.; Das, S. Contact engineering for 2D materials and devices. *Chem. Soc. Rev.* **2018**, *47*, 3037–3058.

[S9] Goryca, M.; Li, J.; Stier, A. V.; Taniguchi, T.; Watanabe, K.; Courtade, E.; Shree, S.; Robert, C.; Urbaszek, B.; Marie, X.; Crooker, S. A. Revealing exciton masses and dielectric properties of monolayer semiconductors with high magnetic fields. *Nat. Commun.* **2019**, *10*, 4172.

[S10] Morozov, S.; Wolff, C.; Mortensen, N. A. Room-Temperature Low-Voltage Control of Excitonic Emission in Transition Metal Dichalcogenide Monolayers. *Adv. Opt. Mater.* **2021**, *9*, 2101305.

[S11] Le Moal, E.; Marguet, S.; Rogez, B.; Mukherjee, S.; Dos Santos, P.; Boer-Duchemin, E.; Comtet, G.; Dujardin, G. An Electrically Excited Nanoscale Light Source with Active Angular Control of the Emitted Light. *Nano Lett.* **2013**, *13*, 4198–4205.

[S12] GutiÃľrrez-Lezama, I.; Ubrig, N.; Ponomarev, E.; Morpurgo, A. F. Ionic gate spectroscopy of 2D semiconductors. *Nat. Rev. Phys.* **2021**, *3*, 508–519.

[S13] Li, Q.; Song, J.; Besenbacher, F.; Dong, M. Two-Dimensional Material Confined Water. *Acc. Chem. Res.* **2015**, *48*, 119–127.